https://doi.org/10.3311/PPci.20342

Periodica Polytechnica Civil Engineering, 66(4), pp. 1133–1143, 2022

Investigation of Cutting Rock by TBM Hob using a SPG Method

Xuhui Zhang[1], Tao Tan[1], Dingbang Hu[1], Mi Li[1*], Laikuang Lin[2], Shun Lin[3]

[1] College of Engineering and Design, Hunan Normal University, Changsha 410081, China
[2] College of Mechanical and Electrical Engineering, Central South University, Changsha Hunan 410083, China
[3] Shuda College, Hunan Normal University, Changsha 410017, China
[*] Corresponding author, e-mail: limi_gsy@hunnu.edu.cn

Received: 19 April 2022, Accepted: 22 July 2022, Published online: 15 August 2022

Abstract

TBM (tunnel boring machine) hob is the core component of the TBM for rock cutting, whose cutting performance can directly determine the overall tunneling efficiency of the TBM. The understanding of cutting rock caused by TBM hobs is still not enough due to the complex contact features between the TBM hob and rock. To study the dynamic cutting process of the TBM hobs deeply, the rock cutting numerical model of the TBM hob is built based on the SPG (smooth particle Galerkin) method, the influence of hob penetration and hob spacing on rock breaking dynamic process, rock cutting forces and specific energy consumption are investigated. The results indicate that the dynamic process of sequential cutting of TBM hobs can be simulated well, and the rock breaking patterns caused by TBM hobs can be reflected with the SPG method. It also shows that the cutting forces of the hob are positively correlated with the hob penetration and hob spacing. For a given hob penetration, there exists an optimum hob spacing to acquire the highest rock cutting efficiency. The hob penetrations of 5, 7, 9, and 11 mm correspond to the optimum hob spacing of 60, 80, 90, and 100 mm respectively. Finally, the simulated results based on the SPG method are verified by comparing the experimental results and the CSM model. This study can provide a new method for simulating the rock cutting dynamic process of the TBM hobs.

Keywords

TBM hob, SPG, hob penetration, hob spacing

1 Introduction

TBM (Tunnel boring machine), large and complex equipment, is widely used in various large-scale tunnel construction projects, which has the advantages of high comprehensive efficiency, fast tunneling speed, and environmental protection [1–3]. The cutting performance of the TBM hob has an important impact on important performance indicators of the TBM, such as boring speed and excavation efficiency [4, 5]. The study about the cutting characteristics of the TBM hob is mainly derived from the field excavation test, the indoor cutting test, and the numerical simulation [6–8]. Field test of cutting rock by TBM hob during tunneling process is the most authentic and reliable method, but it is often limited by actual operating conditions, in which the cutting process and cutting forces are difficult to obtain. Rock cutting test of the TBM hob in the indoor laboratory is a feasible means, but it is time-consuming and cost-consuming for the massive cutting attempts. In recent years, with the rapid progress of computer simulation technology, some rock cutting simulations around the TBM hob are introduced, such as finite element simulation and discrete element simulation methods.

In terms of the finite element method, Cho et al. [9] investigated cutting forces and the optimum cutting spacing of the TBM hob by using AUTODYN-3D. Yang et al. [10] discussed the rock-cutter interaction characteristics through LS-DYNA. Geng et al. [11] simulated the rock breaking process caused by the TBM hob according to a new rock material definition in ABAQUS. Li et al. [12] obtained the stress state of the TBM hob during the rock cutting process with the ANSYS. Zhou et al. [13] carried out the rock cutting simulations by double TBM hobs based on ABAQUS. Xia et al. [14] analyzed the impacts of the free surface on the rock breaking characteristics caused by the TBM hob through AUTODYN-3D. Zhao et al. [15] illustrated the rock cutting performance caused by a cross-section TBM hob with ABAQUS. In terms of the discrete element method. Gong et al. [16] conducted UDEC simulations to achieve the optimum hob spacing. Zare Naghadehi et al. [17] investigated the optimum cutting spacing of the TBM hob considering the joint condition with UDEC. Zhang et al. [18] discussed the effects of the mixed-face ground on the rock cutting features through the PFC. Liu et al. [19] simulated

Cite this article as: Zhang, X., Tan, T., Hu, D., Li, M., Lin, L., Lin, S. "Investigation of Cutting Rock by TBM Hob using a SPG Method", Periodica Polytechnica Civil Engineering, 66(4), pp. 1133–1143, 2022. https://doi.org/10.3311/PPci.20342

the crack propagation caused by different types of TBM hob blades according to PFC. Xue et al. [20] analyzed the rock fragment in joints condition caused by the TBM hob through MatDEM.

The above simulation researches greatly push forward the understanding of the rock cutting characteristics of the TBM hob. However, the cutting simulation technology of the TBM hob still needs to be developed in depth to acquire more accurate cutting results in the simulation. Especially, the cutting forces, crack propagation, and rock failure induced by the TBM hobs are very difficult to simulate since the contact features between the TBM hob and rock are very complex.

The SPG method is proposed to simulate the breaking process of the semi-brittle and ductile material by adopting a new generation meshfree solution. Unlike the traditional FEM (finite element method), which uses elemental erosion techniques to model material separation, the SPG method proposes a bond-based material damage criterion that reproduces the strong discontinuity of the displacement field without sacrificing the conservation properties of the system equations.

Wu et al. [21] studied the impact and penetration problems of three-dimensional concrete with this method, compared their numerical results with experimental data, and showed that the SPG method was steady and convergent during the failure process of the simulated material. Therefore, the SPG method has great potential to simulate the dynamic process of rock failure, as well as display the crack propagation during the cutting process generated by the TBM hobs, and accurately reflect the change rules of cutting forces on the TBM hobs. Consequently, the rock cutting model by TBM hobs is built based on the SPG method, and the influences of the hob penetration and hob spacing on the rock cutting performance of the TBM hobs are studied in this paper. Finally, the simulated results obtained from the SPG method are verified by comparing with the existing crack propagation state results from the cutting test and the rock cutting forces model of CSM (predictive model of Colorado School of Mines). This research could supply a reference for the rock cutting simulation of the TBM hob and promote the development of the rock cutting simulation effectively.

2 Numerical simulation model of rock cutting by TBM hobs

2.1 Establishment of the cutting model by TBM hobs

The sequential cutting model by two TBM hobs is established considering the actual rock cutting process in TBM engineering. The rock sample with a dimension of 300 mm × 400 mm × 600 mm and the TBM hob with a size of 17 inches are formed firstly. For the rock sample, the length in the cutting direction is 600 mm. The TBM hob blade width and angle are about 18 mm and 20°, respectively. Then they are assembled and meshed. Furthermore, the processed files are imported into LS-DYNA for calculation based on the SPG method. The SPG analysis begins with the same discretization of solid elements as the 3D FEM. In the SPG system, all geometry of solid elements can be accepted by the SPG formula, such as tetrahedron, pentahedron, hexahedron, heptahedron, and octahedron.

The "SECID" parameter on the "*PART" card needs to be set to "*SECTION_SOLID_SPG". It has to be noted that "FORM" on the "*SECTION_SOLID_SPG" card should be set as 47 for the SPG analysis [21]. To shorten the simulation time, the grid size of the rock is divided into three layers, and the grid size of the rock mesh from top to bottom is 4 mm, 5 mm, and 6 mm, as illustrated in Fig. 1. Meanwhile, the bottom, right, and left sides of the rock sample are restricted, and these sides are set to non-reflective boundaries to reduce the influence of fixed constraints on cutting force and rock breaking effect. The upper side of the rock sample is available for the TBM hobs to cut. To simulate the relationship between the TBM hobs and the rock truly, the motion mode of the TBM hob is set as passive rotation employing a hinge connection at the center position of the TBM hob, and the contact mode between the TBM hobs and the rock is described by the point-surface contact in LS-DYNA. Geng et al. [22] and Jiang et al. [23] showed that the cutting speed of the hobs has little effect on rock cutting energy and cutting forces when the cutting speed varied in a certain range. Accordingly, the cutting speed of the hobs is set as 25 m/s to reduce the calculation time of the computer. In the simulation process, the TBM hob is set as rigid without considering deformation and material wear. The width between two hobs is described as the hob spacing, and the cutting depth of the TBM hob is denoted as the hob penetration, which is depicted in Fig. 1. The selected values of hob penetration (P) and hob spacing (S) in cutting simulations are shown in Table 1.

2.2 Rock material setting

The red sandstone is adopted as the rock sample and it is described by the RHT (Riedel, Hiermaier, and Thoma) constitutive model [24]. The RHT model introduces three equations related to pressure, namely, yield surface, failure surface, and residual strength surface equations, which

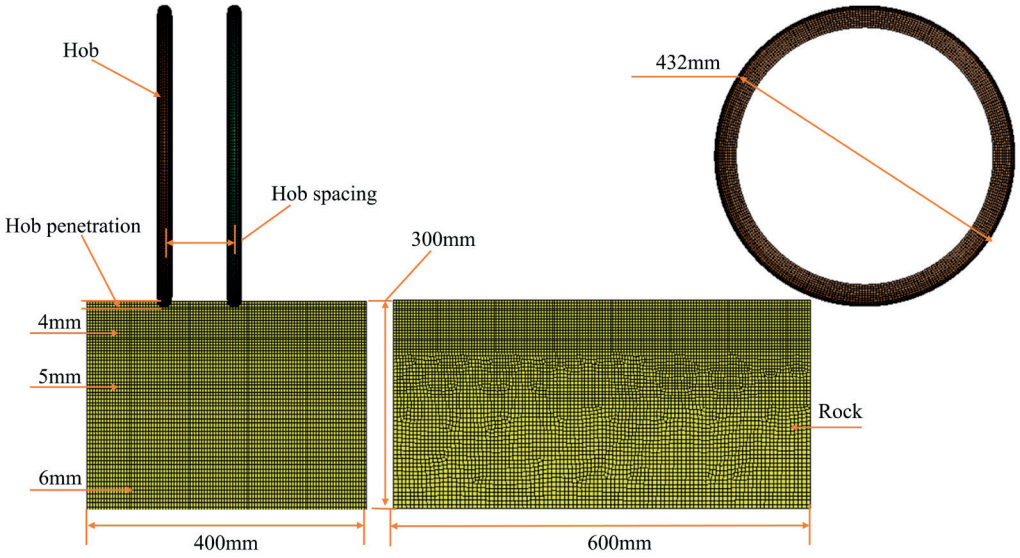

Fig. 1 Rock Cutting model by TBM

Table 1 The selected values of hob penetration and hob spacing in cutting simulations

Hob penetration (mm)	Hob spacing (mm)					
5	50	60	70	80	90	100
7	60	70	80	90	100	110
9	70	80	90	100	110	120
11	80	90	100	110	120	130

respectively describe the changes of initial yield strength, failure strength, and residual strength [25], as illustrated in Fig. 2.

The RHT model can simulate the lateral effect, strain rate effect, and dilatancy effect, so it is suitable for large deformation analyses such as hob penetration and explosion [26]. Its failure surface equation is:

$$\sigma^* = Y^*_{TXC}(P)R_3(\theta)F_{rate}(\dot{\varepsilon}). \tag{1}$$

Here, Y^*_{TXC}, $R_3(\theta)$, $F_{rate}(\dot{\varepsilon})$ represent the compression meridian, corner function and strain rate enhancement factor respectively, which can be expressed as:

$$\begin{cases} Y^*_{TXC}(p) = A[p^* - p^*_{spall}F_{rate}(\overset{\circ}{e})]^N \\ R_3(\theta) = \dfrac{2(1-Q_2^2)cos\theta + (2Q_2-1)[4(1-Q_2^2)cos^2\theta + 5Q_2^2 - 4Q_2]^{\frac{1}{2}}}{4(1-Q_2^2)cos^2\theta + (2Q_2-1)^2} \\ F_{rate}(\overset{\circ}{\varepsilon}) = \begin{cases} (\overset{\circ}{\varepsilon}/\overset{\circ}{\varepsilon}_0)^{\partial} & for \quad p > f_c/3 with \varepsilon_0 = 3.0\times10^{(-6)}s^{-1} \\ (\overset{\circ}{\varepsilon}/\overset{\circ}{\varepsilon}_0)^{\delta} & for \quad p < f_c/3 with \varepsilon_0 = 3.0\times10^{(-6)}s^{-1} \end{cases} \end{cases} \tag{2}$$

Among:

$$\begin{cases} \theta = \dfrac{1}{3}cos^{-1}\left(\dfrac{3\sqrt{3}J_3}{2J_2^{\frac{3}{2}}}\right) & 0 \le \theta \le \dfrac{\pi}{3} \\ Q_2 = \dfrac{r_t}{r_c} = Q_0 + B_0 p^* & 0.51 \le Q_2 \le 1.0 \end{cases} \tag{3}$$

In the above formula, $p^*_{spall} = P_{spall}/f_c$, it represents the normalized spallation strength; r_t and r_c are the partial stresses at the tension meridian and compression meridian respectively; Q_2 is the ratio of deviatoric stress at the meridian of tension and compression; B_0 represents the brittle-ductile transition parameter; A, N, α, δ, and Q_0 are material constants, and their values are generally determined through tests.

Wang et al. [26] Systematically analyzed the meaning of the residual surface, yield surface, and the failure surface of the RHT constitutive model and the meaning of the parameters involved in the RHT constitutive model, and the acquisition method of those parameters in the p–α

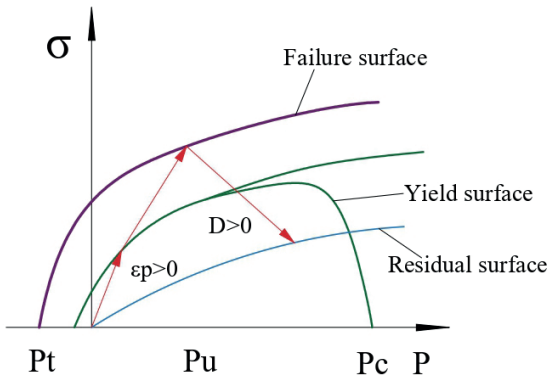

Fig. 2 Three limit surfaces of the RHT constitutive model

state equation. Meanwhile, the performance of the RHT constitutive model in simulating the crack behavior of granite has been verified. Li et al. [24] studied the determination of 15 of the 34 RHT constitutive model parameters that are difficult to determine. Through the orthogonal test method, the RHT constitutive model parameters of red sandstone are obtained, and the correctness of the parameters is verified. Therefore, the above studies confirm that the RHT constitutive model can simulate the rocks well and can also respond well to the crack generation pattern of the rocks. According to the above studies, the key parameters of the red sandstone regarded as the rock sample are shown in Table 2.

Table 2 Material parameters of red sandstone samples

parameters	explanations	Value
f_c/GPa	Compressive strength	0.086
ρ_0/(g/cm^3)	Mass density	2.06
A_2/GPa	Hugoniot polynomial coefficient	26.61
β_t	Tensile strain rate dependence exponent	0.019
B_1	Parameter for polynomial EOS	1.68
T_2/GPa	Parameter for polynomial EOS	0
P_{el}/GPa	Crush pressure	0.0287
$\dot{\varepsilon}_0^t$/10^{-9}ms^{-1}	Reference tensile strain rate	3.0
$\dot{\varepsilon}^t$/10^{-22}ms^{-1}	Break tensile strain rate	3.0
B	Lode angle dependence factor	0.0105
N	Failure surface parameter N	5.8
f_s^*	Relative shear strength	0.45
n_f	Residual surface parameter	0.59
g_c^*	Compressive yield surface parameter	0.3
p_{comp}	Compaction pressure	0.55
ε_p^m	Minimum damaged residual strain	0.01
n	Failure surface parameter N	0.56
α_0	Initial porosity	1.12
A_1/GPa	Hugoniot polynomial coefficient	15.84
A_3/GPa	Hugoniot polynomial coefficient	16.26
B_0	Parameter for polynomial EOS	1.68
T_1/GPa	Parameter for polynomial EOS	15.84
G/GPa	Elastic shear modulus	10.5
$\dot{\varepsilon}_0^c$/10^{-8}ms^{-1}	Reference compressive strain rate	3.0
$\dot{\varepsilon}^c$/10^{-22}ms^{-1}	Break compressive strain rate	3.0
D_2	Damage parameter	1
g_t^*	Tensile yield surface parameter	0.7
Q_0	Lode angle dependence factor	0.54
A_f	Residual surface parameter	1.63
f_t^*	Relative tensile strength	0.1
ξ	Shear modulus reduction factor	0.3
A	Failure surface parameter A	1.6
D_1	Damage parameter	0.053
β_c	Compressive strain rate dependence exponent	0.014

3 Numerical simulation results and analysis

3.1 Dynamic process of cutting rock by TBM hobs

To illustrate the dynamic cutting process of the TBM hobs, the cutting simulation results in a hob penetration of 11 mm, and a hob spacing of 80 mm is taken as an example. Fig. 3 illustrates the dynamic process of the cutting forces including the vertical force (FV) and rolling force (FR), induced by two sequential TBM hobs. The dynamic rock fragmentation condition is shown in Fig. 4 and the vertical cross-sections of the rock at intervals of 25 mm, 50 mm, 250 mm, 300 mm, and 450 mm are labeled as a, b, c, d, and e, respectively. The cutting forces of the preceding hob (the left hob 1 in Fig. 4) are recorded as FV_1 and FR_1, and the cutting forces of the subsequent hob (the right hob 2 in Fig. 4) are recorded as FV_2 and FR_2.

It can be observed from Fig. 3 that the rock cutting process is roughly divided into three stages for each TBM hob. The first stage is the initial stage of cutting rock by the hob, at which the cutting time ranges from 0 to about 0.002 s for the hob 1. At this stage, the hob blade begins to contact the rock sample gradually and the cutting forces also increase steadily, as shown in Fig. 4(a) and Fig. 3. In the meantime, a crushed zone similar to an inverted triangle shape beneath the TBM hob is produced, as depicted in Fig. 4(a). The crushed zone will expand, and the lateral and longitudinal cracks also will initiate and propagate with the continuous movement of the hob 1, as depicted in Fig. 4(b). At the end of the first stage, the contacting area between the hob 1 and the rock sample reaches the maximum, the FV_1 and FR_1 first reach the peaks with values of about 125.31 kN and 27.51 kN respectively. The second stage is the stable rock cutting stage, at which the cutting time varies from about 0.002 s to about 0.028 s for the hob 1. At this stage, the morphology of the crushed zone beneath the TBM hob is similar to the continuous cutting of hob 1, and the cutting forces show a fluctuation feature with the change in cutting time. It can be observed from Fig. 3 that FV_1 fluctuates between about 125.31 kN and 175.54 kN and FR_1 fluctuates between about 21.28 kN and 28.42 kN. The third stage is the cutting end stage, at which the cutting time ranges from about 0.028 s to about 0.034 s for the hob 1. At this stage, the TBM hob will finish the cutting process, the contacting area between the hob 1 blade and the rock, and the cutting forces gradually decrease to 0.

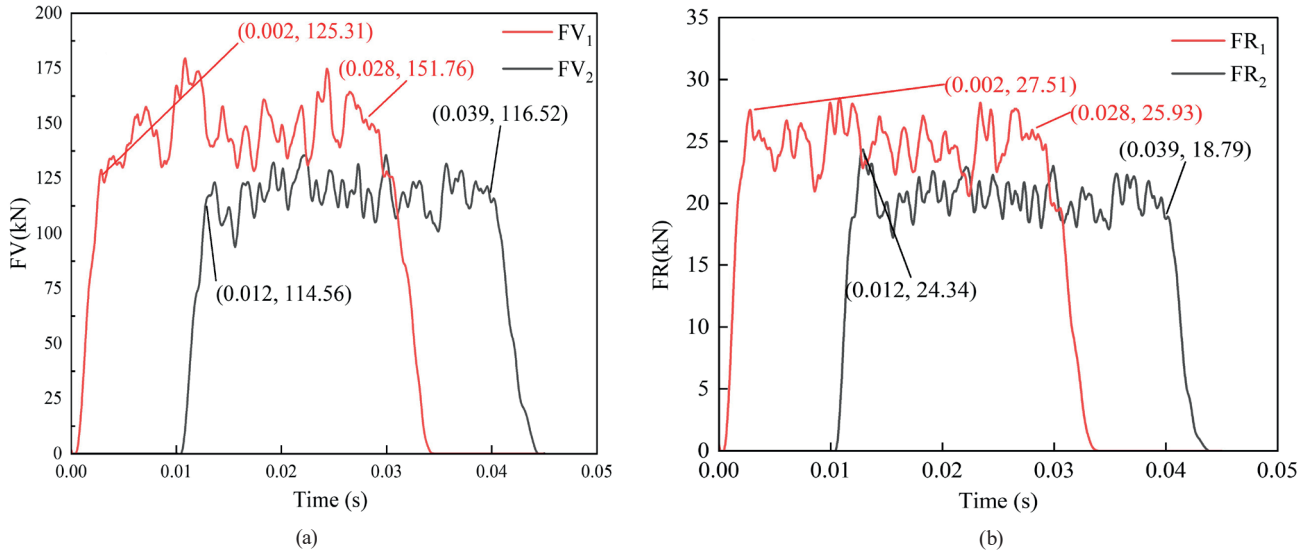

Fig. 3 Variation relationship between cutting forces and cutting time while hob penetration is 11 mm and hob spacing is 80 mm

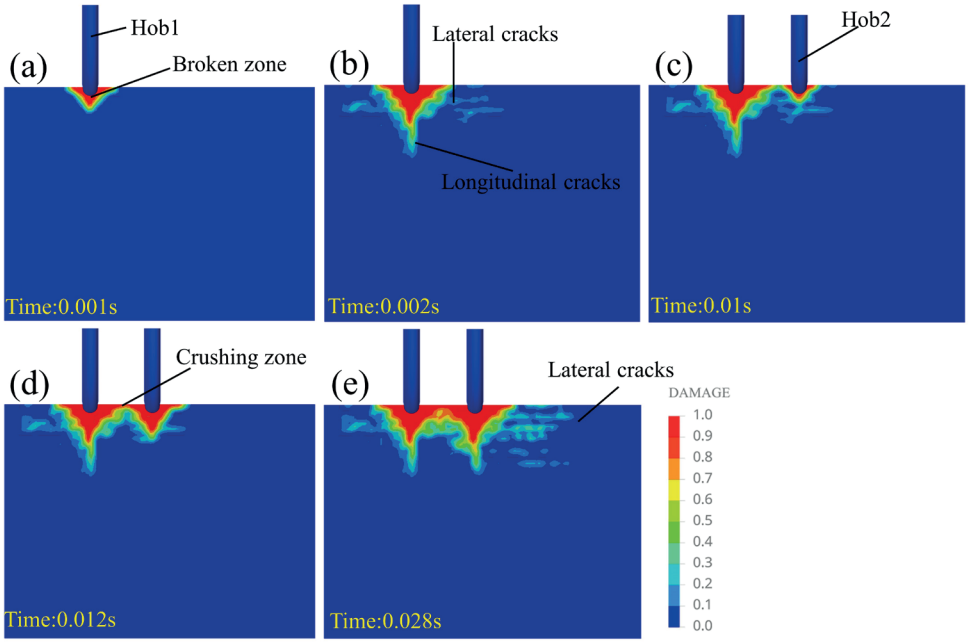

Fig. 4 Dynamic rock breaking process with hob penetration of 11 mm and hob spacing of 80 mm

The cutting process of the subsequent TBM hob (hob 2) also contains three similar stages. The hob 2 starts to cut rock samples at the time of 0.01 s. With the continuous cutting of the hob 2, the crushed zone beneath the hob blade also first expands and then keeps stable at the first two stages, as depicted in Fig. 4(c), (d), and (e). Additionally, it can be observed that the lateral cracks between two TBM hobs can meet with each other and the rock ridge between two TBM hobs can be peeled off, as depicted in Fig. 4(e), indicating that the preceding and subsequent cuts have a synergistic effect to cut rock sample at such hob penetration and hob spacing. Moreover, it can be calculated that the average values of the FV_1 and FR_1 at the stable rock cutting stage are about 144.65 kN and 23.81 kN respectively, while the average values of the FV_2 and FR_2 at the stable rock cutting stage are only about 106.24 kN and 19.51 kN. It implies that the cutting forces caused by hob 2 are much lower than that caused by hob 1. This phenomenon can be explained that hob 2 cuts the rock sample based on the preceding cutting of hob 1, which has produced a cutting groove liking a free surface. Therefore, the free surface can alleviate the cutting condition and reduce the cutting forces of the hob 2.

3.2 Rock breaking states under different hob penetration and hob spacing

To investigate the rock breaking features induced by sequential cutting of the TBM hobs, the external and internal rock breaking patterns at different cutting parameters are analyzed in this section based on the SPG results. Fig. 5(a), (b), and (c) illustrate the external rock breaking states with a given hob penetration of 9 mm and hob spacing of 70, 90, and 120 mm respectively, while Fig. 5(d), (e), and (f) present the external rock breaking states with a given hob spacing of 100 mm and hob penetration of 5, 7, and 11 mm. Fig. 6 shows the internal rock breaking states corresponding to the same cutting condition in Fig. 5.

In the case of the same hob penetration, When the hob spacing remains at a low level, such as 70 mm and 90 mm, the lateral cracks produced by the sequential cutting can

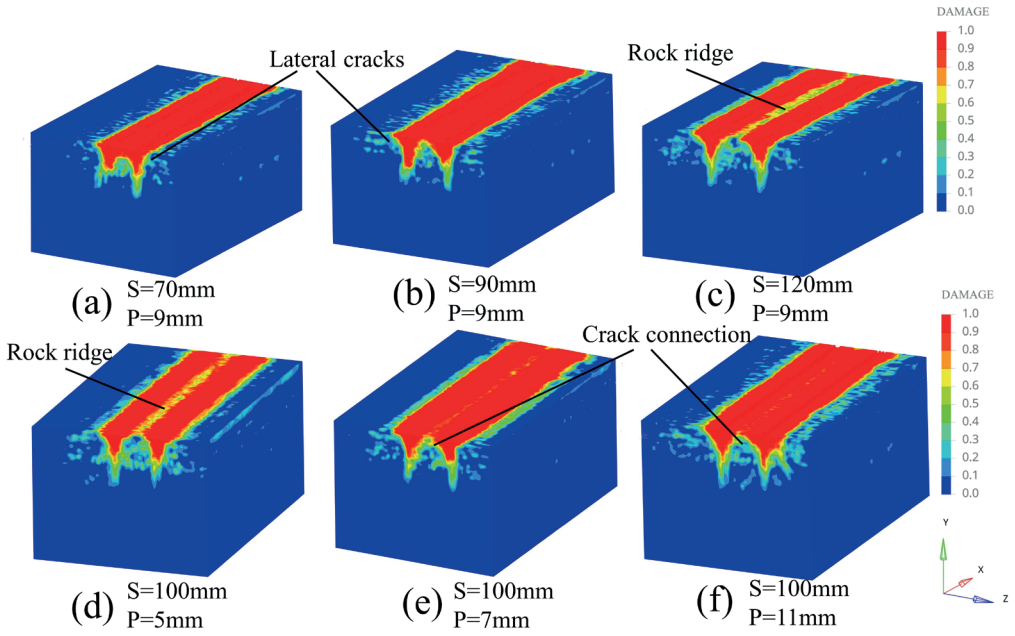

Fig. 5 External rock breaking patterns at different cutting parameters

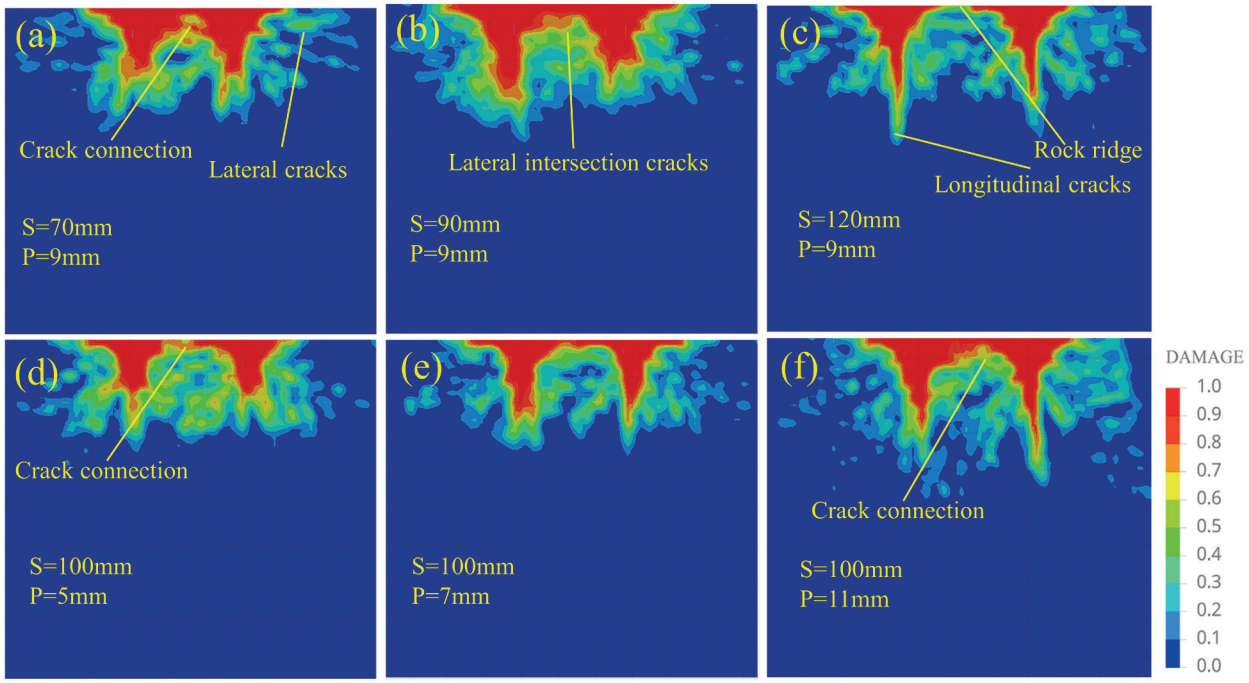

Fig. 6 Internal rock breaking patterns at different cutting parameters

intersect with each other and can cut the rock ridge away, as shown in Fig. 5(a) and (b), Fig. 6(a) and (b). It denotes that the sequential cuttings caused by two TBM hobs have a synergistic impact to cut the rock when the hob spacing is at a low level. In addition, the rock crushed depth between two cuttings gets shallower with the increase of the hob spacing compared to Fig. 6(a) and (b), indicating that larger hob spacing will weaken the intersection of the lateral cracks between two cuttings. This phenomenon can be further observed when the hob spacing is 120 mm for a hob penetration of 9 mm, as presented in Fig. 5(c) and Fig. 6(c), in which the lateral cracks could not intersect with each other and a long rock ridge between two cuttings can be found clearly since the hob spacing is too large to form a synergistic effect between two TBM hobs. Therefore, for a given hob penetration, there is a proper hob spacing for sequential hob cutting to cut the rock ridge away. If the hob spacing is too small, the rock crushed volume is too small, and if the hob spacing is too large, the mutual cooperative cutting by TBM hobs disappears and the rock ridge appears. For the circumstance of the same hob spacing, when the hob penetration keeps at a low level, such as 5 mm, an obvious rock ridge along the cutting direction can be found since the lateral cracks between two cutting grooves could not connect each other, as presented in Fig. 5(d) and Fig. 6(d). However, with the increase of the hob penetration, the rock ridge begins to fade away and the crushed depth between two cuttings becomes deeper, as shown in Fig. 5(e) and (f), Fig. 6(e) and (f). It indicates that the interaction extent between the two TBM hobs will become more obvious with the increase of the hob penetration.

According to the above analysis of the rock breaking states, it can be concluded that the hob penetration and hob spacing significantly influence the crack propagation and the rock breaking features. Thus, the proper cutting parameters, namely hob penetration and hob spacing, play a significant role in raising the rock cutting efficiency of the TBM hobs, which will be further analyzed in the next sections.

3.3 Rock cutting forces under different hob penetration and hob spacing

The average cutting forces of hob 2 under different cutting parameters are collected in Fig. 7 according to the simulated results. Overall, both the FV and the FR increase stably with the ascent of the hob spacing and hob penetration. Taking the FR as an example, it increases from 19.89 kN to 23.79 kN when the hop spacing increases from 80 mm

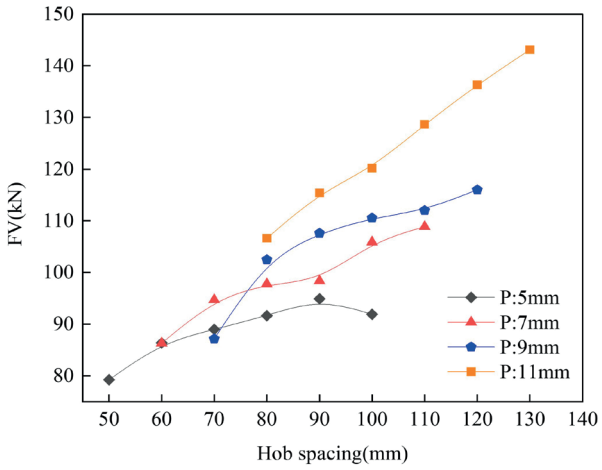

(a)

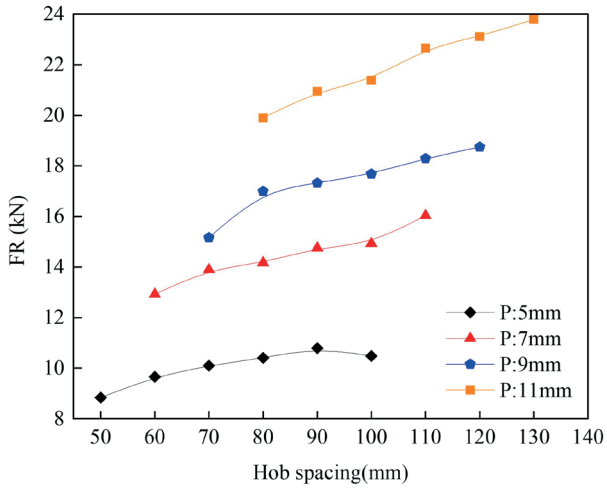

(b)

Fig. 7 Variation of rock cutting force with hob spacing: (a) FV; (b) FR

to 130 mm for the given hob penetration of 11 mm. In the meantime, the FR grows from 10.79 kN to 20.95 kN as the hop penetration increases from 5 mm to 11 mm for the given hob spacing of 90 mm. It should be pointed out that the FV with the hob penetration of 9 mm is lower than that of 5 mm for the given hop spacing of 70 mm, as shown in Fig. 7(a). It can be explained that hob 1 with a hob penetration of 9 mm has cut a deeper groove compared with that of 5 mm, causing greater damage in the rock sample which can relieve the FV of hob 2 for a narrow hop spacing of 70 mm. Therefore, the hob 2 with the hob penetration of 9 mm may cut rock with less force compared with that of 5 mm, resulting in a lower FV. In addition, for the given hob penetration of 5 mm, the FV and FR remain at a relatively stable value when the hop spacing exceeds 90 mm. It can be interpreted that the rock ridge will appear while the hop spacing exceeds 90 mm for the hob penetration of 5 mm, resulting in similar cutting conditions and similar

cutting force for hob 2. It also can be discovered that the FV is much larger than the FR at the same cutting parameter, the former is roughly 5–9 times as large as the latter, indicating that the FV plays a dominant role in the cutting rock process.

3.4 Rock cutting efficiency under different hob penetration and hob spacing

The SE (specific energy consumption) is the consumed energy of the TBM hob to cut rock per unit volume, and it is widely used to assess the cutting efficiency of the TBM hob. The lower the specific energy, the higher the cutting efficiency. Its calculation formula is

$$SE = \frac{FR \cdot L}{V}, \tag{4}$$

where L is the hob cutting length, m, FR is the rolling force, and V is the crushed volume of the rock sample.

As can be seen in Fig. 6, the crushed region of the rock represents the portion of the damage that exceeds 0.8, and this portion of the volume is attributed to crushed rock. Fig. 8 presents the changing trend of the SE with different hob penetration and hob spacing based on the simulated results. Overall, the SE decreases firstly and subsequently increases with the rise of the hob spacing regardless of the hob penetration. For instance, at the penetration of 9 mm, the SE will arrive at the valley with a value of 38.1 MJ/m^3 when the hob spacing increases to 90 mm. It can be interpreted that the crushed volume of the rock between two cutting grooves generated by the sequential hobs is at a low level when the hob spacing is narrower than 90 mm (Fig. 5(a) and Fig. 6(a)), and the rock between two cutting grooves are excessively crushed due to the large violent interaction between the preceding and subsequent cuttings, leading to a larger SE. While the hob spacing is wider than 90 mm, the interaction between the preceding and subsequent cuttings is disappeared and a rock ridge is left (Fig. 5(c) and Fig. 6(c)), causing growth in SE compared with that at the hob spacing of 90 mm. It demonstrates that it exists an optimum hob spacing to reach the highest rock cutting efficiency, which is corresponding to the lowest SE for a given hob penetration. The optimum hob spacing is 60, 80, 90, and 100 mm respectively as the hob penetration is 5, 7, 9, and 11 mm. For the given hob spacing, the SE corresponding to the hob penetration of 5 mm seems to have the lowest cutting efficiency with a large SE. There is no obvious feature about the SE with other hob penetrations. It implies that hob penetration and hob spacing may have a comprehensive impact on the SE. This will be investigated in the next section considering the ratio of hob spacing and hob penetration.

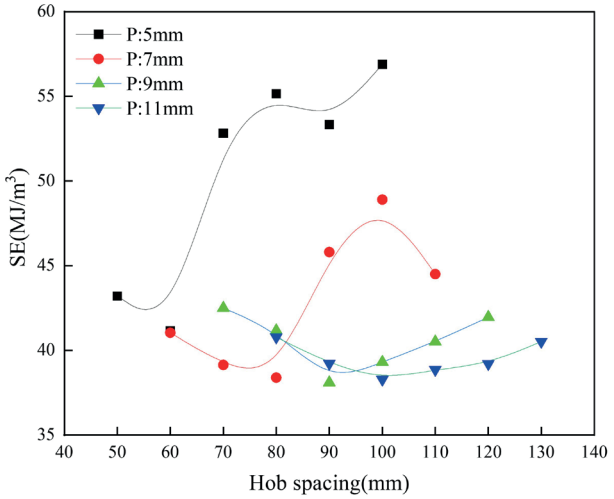

Fig. 8 Variation of the specific energy with hob spacing

3.5 Influence of the ratio of hob spacing and hob penetration on rock cutting efficiency

To investigate the comprehensive influence of the hob spacing and hob penetration on the rock cutting efficiency, the relationship between the SE and the ratio of the hob spacing to hob penetration (S/P) is summarized in Fig. 9. With the growth of the S/P, the SE shows a trend of first decreasing and then increasing, and the lowest SE with a value of approximately 38.10 MJ/m^3 is achieved while the S/P is at around 10. Interestingly, the TBM hob can acquire the highest cutting efficiency when cutting rock at such S/P with a value of around 10. It can also be found that the SE corresponding to a large S/P (more than 15) is much higher than that corresponding to a small S/P (less than 15). It was mainly caused by the weak interaction

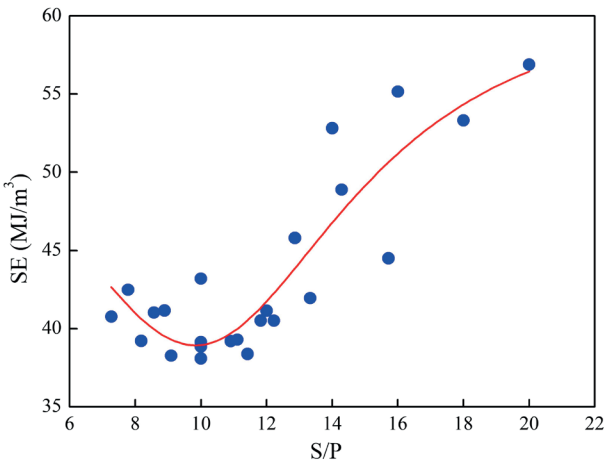

Fig. 9 The relationship between SE and S/P

between the preceding cutting and subsequent cutting of the TBM hobs, and these two TBM hobs could not cooperate to cut rock each other at such large S/P (more than 15). Therefore, cutting rock with a relatively small S/P is more conducive than that with a relatively large S/P considering the cutting efficiency of the hob.

4 Discussion and verification

The simulated results are compared with the existing experimental and theoretical results in this section to verify the effectiveness of these simulated results with the SPG method. Entacher et al. [27] presented a series of crushed morphology beneath the TBM hob in the cutting direction according to the cutting experiments, as displayed in Fig. 10(a). Fig. 10(b) displays the crushed morphology beneath the hob 1 for 10 mm and 30 mm cutting length obtained from the SPG method. An inverted triangular crushed zone beneath the hob blade can be found in both the experimental and simulated results, and some minor cracks around the inverted triangular crushed zone can also be observed in both results. It implies that the rock breaking process under the TBM hob can be simulated and reflected well with the SPG method.

To verify the reliability of the rock cutting forces of the TBM hob acquired from the SPG method, the cutting forces including the FV and the FR analyzed in Section 3.3 are compared with the CSM theoretical model. The CSM model is proposed by the Colorado School of Mines, which has been widely used in the TBM engineering field. This model can predict the FV and the FR respectively [28, 29], which are shown below.

$$FV = TR\phi C\sqrt[3]{\frac{S\sigma_C^2\sigma_t}{\phi\sqrt{RT}}}Cos(\frac{\phi}{2}), \tag{5}$$

$$FR = TR\phi C\sqrt[3]{\frac{S\sigma_C^2\sigma_t}{\phi\sqrt{RT}}}Sin(\frac{\phi}{2}), \tag{6}$$

where ϕ denotes the contacting angle between the hob blade and the rock; R denotes the radius of TBM hob; T denotes the edge width of hob; C denotes the dimensionless coefficient, which is generally 2.12; S denotes the hob spacing; σ_c denotes the uniaxial compressive strength of the rock sample; σ_t denotes the tensile strength of the rock sample.

According to the above formulas, the cutting forces of the CSM model are acquired when cutting the sandstone mentioned in Section 2.2. The comparison of the FV and FR between the CSM model and the simulated results is illustrated in Fig. 11. The average fitting ratio of the FV from the CSM model and the simulated results is 0.978, as presented in Fig. 11(a). The average fitting ratio of the

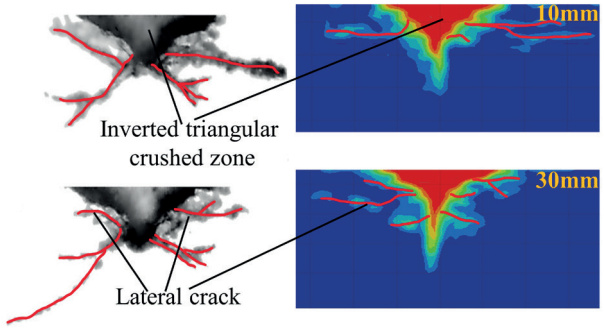

(a) (b)

Fig. 10 (a) Cross-sections of rock test result [27], (b) Cross-sections of rock of numerical simulation

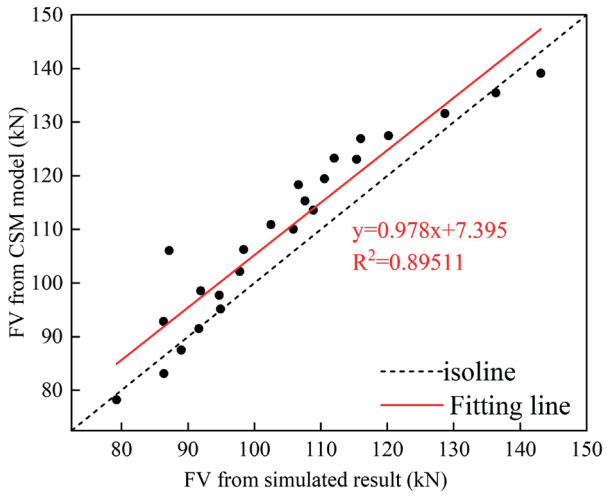

(a)

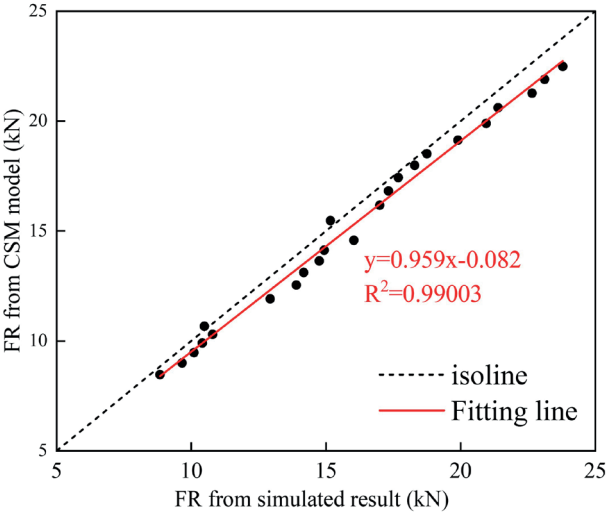

(b)

Fig. 11 Comparison between simulation results and CSM theoretical model calculation data results

FV and the centralized distribution of data points present a close relationship between the CSM model and the simulated results, although the FV from the simulated results is slightly lower than that from the CSM model. For the FR of the TBM hob, the fitting ratio between the CSM model and simulated results is 0.959, as shown in Fig. 11(b). The data points of the FR are densely distributed and concentrated on the isoline. In short, the cutting forces obtained from the simulated results are very close to that from the CSM model. Thus, the simulated results based on the SPG method can reflect and calculate the cutting forces of the TBM hob well.

In conclusion, the SPG method can effectively simulate the dynamic cutting process of the TBM hobs, the crushed pattern beneath the TBM hob can be reflected well, and the obtained rock cutting force is also reliable. Thus, the rock cutting simulation of the TBM hobs using the SPG approach can serve as a strong benchmark and the simulated results are steady and dependable.

5 Conclusions

To investigate the dynamic cutting process of the TBM hobs, the cutting model based on the SPG method is established, the rock cutting characteristics under different hob penetration and hob spacing are studied, and the main conclusions are presented as follows.

1. The dynamic cutting process of each TBM hobs can be divided into three stages in these simulations according to the dynamic cutting forces. The crushed zone shows an inverted triangle shape beneath the TBM hob during the cutting process. Furthermore, the cutting forces show a fluctuation feature in the stable rock cutting stage. The cutting forces of the subsequent hob can be improved by the cutting groove produced by the preceding TBM hob.
2. The SPG simulation method can well reflect the rock breaking states. There is a synergistic impact for the same hob penetration to cut away the rock ridge between two cuttings when the hob spacing is low. Then, the synergistic impact of the cuttings will disappear, and the rock ridge will be formed when the hob spacing arrives at a high level. For the same hob spacing, the hob penetration with a large value can deepen the crushed zone and enhance the interaction of two cuttings of the TBM hob.
3. The cutting forces grow steadily with the increase of the hob spacing and hob penetration on the whole, and the FV is about 5–9 times more than the rolling force FR at the same cutting parameter.
4. An optimum hob spacing exists for a given hob penetration to acquire the highest cutting efficiency. The optimum hob spacing is 60, 80, 90, and 100 mm respectively when the hob penetration is 5, 7, 9, and 11 mm. Considering the Combined effects of the hop spacing and hop penetration, the optimum S/P corresponding to the highest cutting efficiency is around 10.
5. The crushed pattern beneath the TBM hob obtained in simulation is similar to the experimental results, and the cutting forces obtained in simulation can match well with the CSM model, which demonstrated the feasibility and reliability of the SPG method.

Acknowledgments

Thanks for the support of the following projects: the National Natural Science Foundation of China (Granted No. 52005179), the Natural Science Foundation of Hunan Province (Granted No.2020JJ5365), the Scientific Research Project of Hunan Education Department (Granted No. 20C1153), and the Innovative Training Program for College students in China (Granted No. S202112652001).

References

[1] Yang, M., Xia, Y., Lin, L., Qiao, S., Ji, Z. "Optimal design for buckets layout based on muck removal analysis of TBM cutterhead", Journal of Central South University, 27, pp. 1729–1741, 2020. https://doi.org/10.1007/s11771-020-4403-1

[2] Zhang, X., Liao, Y., Chen, Z., Xia, Y., Zhang, K. "Study on Optimum Free-face Condition of Cutting Hard Rock with Tunnel Boring Machine Hob", Periodica Polytechnica Civil Engineering, 65(2), pp. 510–521, 2021. https://doi.org/10.3311/PPci.17567

[3] Song, K., Yang, H., Xie, J., Karekal, S. "An Optimization Methodology of Cutter-Spacing for Efficient Mechanical Breaking of Jointed Rock Mass", Rock Mechanics and Rock Engineering, 2022. https://doi.org/10.1007/s00603-022-02806-x

[4] Wang, Z., Liu, C., Jiang, Y., Dong, L., Wang, S. "Study on Wear Prediction of Shield Disc Cutter in Hard Rock and Its Application", KSCE Journal of Civil Engineering, 26, pp. 1439–1450, 2022. https://doi.org/10.1007/s12205-021-0817-z

[5] Lin, Q., Cao, P., Cao, R. "Experimental investigation of jointed rock breaking under a disc cutter with different confining stresses", Comptes Rendus Mécanique, 346(9), pp. 833–843, 2018. https://doi.org/10.1016/j.crme.2018.06.012

[6] Pan, Y., Liu, Q., Liu, Q., Bo, Y., Liu, J., Peng, X., Cai, T. "Comparison and correlation between the laboratory, semi-theoretical and empirical methods in predicting the field excavation performance of tunnel boring machine (TBM)", Acta Geotechnica, 17, pp. 653–676, 2022. https://doi.org/10.1007/s11440-021-01228-3

[7] Liu, J., Cao, P., Jiang, Z., Zhao, Y., Cao, R. "Numerical simulation on effects of embedded crack on rock fragmentation by a tunnel boring machine cutter", Journal of Central South University, 21, pp. 3302–3308, 2014.
https://doi.org/10.1007/s11771-014-2303-y

[8] Huang, X., Liu, Q., Chen, L., Pan, Y., Liu, B., Kang, Y., Liu, X. "Cutting force measurement and analyses of shell cutters on a mix-shield tunnelling machine", Tunnelling and Underground Space Technology, 82, pp. 325–345, 2018.
https://doi.org/10.1016/j.tust.2018.08.052

[9] Cho, J.-W., Jeon, S., Yu, S.-H., Chang, S.-H. "Optimum spacing of TBM disc cutters: A numerical simulation using the three-dimensional dynamic fracturing method", Tunnelling and Underground Space Technology, 25(3), pp. 230–244, 2010.
https://doi.org/10.1016/j.tust.2009.11.007

[10] Yang, H., Wang, H., Zhou, X. "Analysis on the Rock-Cutter Interaction Mechanism During the TBM Tunneling Process", Rock Mechanics and Rock Engineering, 49, pp. 1073–1090, 2016.
https://doi.org/10.1007/s00603-015-0796-9

[11] Geng, Q., Wei, Z., Ren, J. "New rock material definition strategy for FEM simulation of the rock cutting process by TBM disc cutters", Tunnelling and Underground Space Technology, 65, pp. 179–186, 2017.
https://doi.org/10.1016/j.tust.2017.03.001

[12] Li, J., Nie, Y., Fu, K., Ma, C., Guo, J., Xu, M. "Experiment and analysis of the rock breaking characteristics of disc cutter ring with small edge angle in high abrasive grounds", Journal of the Brazilian Society of Mechanical Sciences and Engineering, 40, 505, 2018.
https://doi.org/10.1007/s40430-018-1422-z

[13] Zhou, P., Guo, J., Sun, J., Zou, D. "Theoretical Research and Simulation Analysis on the Cutter Spacing of Double Disc Cutters Breaking Rock", KSCE Journal of Civil Engineering, 23, pp. 3218–3227, 2019.
https://doi.org/10.1007/s12205-019-1777-4

[14] Xia, Y. M., Guo, B., Cong, G. Q., Zhang, X. H., Zeng, G. Y. "Numerical simulation of rock fragmentation induced by a single TBM disc cutter close to a side free surface", International Journal of Rock Mechanics and Mining Sciences, 91, pp. 40–48, 2017.
https://doi.org/10.1016/j.ijrmms.2016.11.004

[15] Zhao, J.-L., Zhu, X. Y., Hou, Z.-H., Liu, C., Yang, S., Xiao, X. "Design and finite element analysis of a variable cross-section cutter ring", Simulation Modelling Practice and Theory, 115, 102423, 2022.
https://doi.org/10.1016/j.simpat.2021.102423

[16] Gong, Q. M., Zhao, J., Hefny, A. M. "Numerical simulation of rock fragmentation process induced by two TBM cutters and cutter spacing optimization", Tunnelling and Underground Space Technology, 21(3–4), p. 263, 2006.
https://doi.org/10.1016/j.tust.2005.12.124

[17] Zare Naghadehi, M., Mikaeil, R. "Optimization of Tunnel Boring Machine (TBM) Disc Cutter Spacing in Jointed Hard Rock Using a Distinct Element Numerical Simulation", Periodica Polytechnica Civil Engineering, 61(1), pp. 56–65, 2017.
https://doi.org/10.3311/PPci.9521

[18] Zhang, Z., Zhang, K., Dong, W., Zhang, B. "Study of Rock-Cutting Process by Disc Cutters in Mixed Ground based on Three-dimensional Particle Flow Model", Rock Mechanics and Rock Engineering, 53, pp. 3485–3506, 2020.
https://doi.org/10.1007/s00603-020-02118-y

[19] Liu, J., Wan, W., Xie, S., Wang, J. "Indentation Characteristics Using Various Indenters: A Study Based on Laboratory and Numerical Tests", Geotechnical and Geological Engineering, 37(6), pp. 4919–4931, 2019.
https://doi.org/10.1007/s10706-019-00952-8

[20] Xue, Y., Zhou, J., Liu, C., M. Shadabfar, M., Zhang, J. "Rock fragmentation induced by a TBM disc-cutter considering the effects of joints: A numerical simulation by DEM", Computers and Geotechnics, 136, 104230, 2021.
https://doi.org/10.1016/j.compgeo.2021.104230

[21] Wu, C. T., Wu, Y., Crawford, J. E., Magallanes, J. M. "Three-dimensional concrete impact and penetration simulations using the smoothed particle Galerkin method", International Journal of Impact Engineering, 106, pp. 1–17, 2017.
https://doi.org/10.1016/j.ijimpeng.2017.03.005

[22] Geng, Q., Wei, Z., Meng, H., Chen, Q. "Numerical and experimental research on the rock-breaking process of tunnel boring machine normal disc cutters", Journal of Mechanical Science and Technology, 30, pp. 1733–1745, 2016.
https://doi.org/10.1007/s12206-016-0329-9

[23] Jiang, B., Zhao, G.-F., Gong, Q., Zhao, X.-B. "Three-dimensional coupled numerical modelling of lab-level full-scale TBM disc cutting tests", Tunnelling and Underground Space Technology, 114, 103997, 2021.
https://doi.org/10.1016/j.tust.2021.103997

[24] Li, H., Chen, Y., Liu, D., Huang, D., Zhao, L. "Sensitivity and Determination Method of Main Parameters of Rock RHT Model", Journal of Beijing Institute of Technology, 38(08), pp. 779–785, 2018. (in Chinese)
https://doi.org/10.15918/j.tbit1001-0645.2018.08.002

[25] Yang, J., Liu, K., Li, X., Liu, Z. "Stress initialization methods for dynamic numerical simulation of rock mass with high in-situ stress", Journal of Central South University, 27(10), pp. 3149–3162, 2020.
https://doi.org/10.1007/s11771-020-4535-3

[26] Wang, Z., Wang, H., Wang, J., Tian, N. "Finite element analyses of constitutive models performance in the simulation of blast-induced rock cracks", Computers and Geotechnics, 135, 104172, 2021.
https://doi.org/10.1016/j.compgeo.2021.104172

[27] Entacher, M., Schuller, E., Galler, R. "Rock Failure and Crack Propagation Beneath Disc Cutters", Rock Mechanics and Rock Engineering, 48, pp. 1559–1572, 2015.
https://doi.org/10.1007/s00603-014-0661-2

[28] Rostami, J. "Study of pressure distribution within the crushed zone in the contact area between rock and disc cutters", International Journal of Rock Mechanics and Mining Sciences, 57, pp. 172–186, 2013.
https://doi.org/10.1016/j.ijrmms.2012.07.031

[29] Xia, Y., Guo, B., Tan, Q., Zhang, X., Lan, H., Ji, Z. "Comparisons Between Experimental and Semi-theoretical Cutting Forces of CCS Disc Cutters", Rock Mechanics and Rock Engineering, 51, pp. 1583–1597, 2018.
https://doi.org/10.1007/s00603-018-1400-x